Multidimensional aware subfaced-based Finite Volume scheme for the Eulerian droplet system of equation

H. Beaugendre, A. Chan, V. Delmas, Raphaël Loubère, P.-H. Maire, F. Morency, T. Vigier

Multidimensional aware subfaced-based Finite Volume scheme for the Eulerian droplet system of equation

H. Beaugendre[a], A. Chan[b,c], V. Delmas[b,c], R. Loubère[b], P.-H. Maire[c], F. Morency[d], T. Vigier[b]

[a] *Institut de Mathématiques de Bordeaux (IMB), Université de Bordeaux, CNRS UMR 5251, Bordeaux INP and INRIA, F-33400, Talence, France*
[b] *Institut de Mathématiques de Bordeaux (IMB), Université de Bordeaux, CNRS UMR 5251, Bordeaux INP, F-33400, Talence, France*
[c] *CEA Cesta, 15 Avenue des Sablières, F-33116, Le Barp cedex, France.*
[d] *Ecole de Technologie Supérieure (ETS), Montreal, Quebec, H3C 1K3, Canada*

Abstract

In clouds and under cold weather, water droplets impact and freeze on aircraft structures. The Eulerian model for the droplet flow predicts the impinging water mass. The model equations are close to the Euler equations but without the pressure term, known as pressureless Euler model. Consequently, the resulting system is only weakly hyperbolic and standard Riemann solvers strongly relying on the eigenstructure of the system cannot solve the Eulerian model. To circumvent this problem, the model is supplemented with an extra-term mimicking the divergence of a particle pressure. The main purpose of this work is to implement a multidimensional aware Riemann solver for a Finite Volume simulation code for the modified formulation of the Eulerian droplet model. The numerical method should preserve physical properties such as the positivity of the liquid water content, and must produce accurate results without sacrificing the general robustness. The flow around a cylinder assess the numerical method in 2D on radial meshes.

Key words: Multi-phase flow, Pressureless Euler equations, multi-dimensional aware Riemann solver, Finite Volume scheme, In-flight icing.

1. Introduction

In-flight icing causes many crashes and accidents, as much as 8% of regional aircraft deathly accident [1]. Ice accretion on aircraft lifting structures induces a drag increase, a loss of lift, and a reduction of the stall angle [2]. This performance degradation, especially if sudden, is the cause of many accidents [3]. Ice accretion can also occur on engine air intakes, spinners and inlet fan blades. Frozen fan blades induce overload and unbalanced mass that would degrade the engine immediately. When this ice breaks away, and is ingested through the remainder of the propulsion system (engine and nacelle), it creates multiple damages.

*Corresponding author
Email addresses: heloise.beaugendre@math.u-bordeaux.fr (H. Beaugendre), vincent.delmas@u-bordeaux.fr (V. Delmas), raphael.loubere@math.u-bordeaux.fr (R. Loubère), pierre-henri.maire@cea.fr (P.-H. Maire)

These damages have a serious negative impact on the operating costs and may also generate some incident concern [4, 5]. To minimize ice accretion, wings and propulsion systems have Ice Protection Systems (IPS) which mostly use air-heated technology through engine bled offs [6, 7]. Air-heated IPS carry associated design penalties and have themselves performance issues. If manufacturers use too cautious design margins, it leads to conservative non-optimized solutions.

The conception of aircraft IPS requires the prediction of areas impacted in-flight by cloud droplets. Critical aircraft surfaces where droplets impinge are prone to aircraft icing and must be protected. In clouds, the airflow around the wing transports suspended water droplets. Due to their high inertia, they impact aircraft surfaces and may freeze. The mass loading, i.e. the bulk density of the droplets over the bulk density of air, is of the order of 10^{-3} in icing conditions. The gas-particle flow is dilute and controlled by local aerodynamic forces. The droplets do not collide, and particle information is not transmitted by particle-particle collision, leading to the absence of a particle pressure. The gas-particle flow in this situation can be modelled using a one-way coupling algorithm since the droplet effects on the airflow is negligible because of the low liquid water content [8, 9]. Generally, one-way coupling is valid if the mass loading is smaller than 0.1 [10].

The classical way to compute impingement in icing, is first to compute the air flow solution. This solution can be obtained solving Euler or Navier-Stokes equations. Taking into account air density and velocity, the droplets trajectory and impact are then computed. Since the objective of this paper is to test the proposed mutidimensional scheme solving the droplets model, then the air flow solution is simply computed using Euler equations, neglecting viscous effects. Computing an inviscid air flow solution is commonly done in icing community, see [11, 12]. Possibly using a turbulent airflow solution may have an impact on shadow zones behind the bodies, but this is beyond the scope of this paper.

For droplet diameters smaller than $100\,\mu m$, many works investigated the equation for droplet motion in airflow [13]. The spherical drag coefficient links the droplet momentum to the airflow. The gravity force can also be involved in large droplets or low air velocity flows. Early numerical icing codes use a Lagrangian coordinate system attached to the droplet [14, 15]. Instead, the CFD codes use an Eulerian coordinate system to solve for the droplet velocity $\mathbf{u}$ and the volume fraction of water ρ [9, 16, 17]. Compared to the Lagrangian method, the Eulerian method does not make a priory estimate on the location of the impingement region and enables the identification of shadow areas [18]. In the shadow areas downstream of the aircraft, the droplets vanish. However, for simple cases, the calculation cost of the Eulerian method is higher when compared to the Lagrangian method. Still, high order implicit solvers, at least second order, enabling large CFL numbers can reduce the computational efforts.

The Eulerian droplet equation system is a particular form of the pressureless gas. The pressureless

gas equations are often used to model clouds of dust [19, 20], with ρ the dust density and $\mathbf{u}$ the velocity. The pressureless gas equations are weakly hyperbolic and the Jacobian matrix is not diagonalizable. The development of delta-shocks, and the emergence of the vacuum state characterize this weakly hyperbolic system.

First order and second order schemes are developed to solve the pressureless gas equations, such as the schemes based on the kinetic approximations [21], the relaxation methods [22], or central schemes [23]. Recently, [24, 25] used the theory of Jordan canonical forms to solve the weakly hyperbolic systems and derive an upwind scheme. The addition of a perturbation parameter ϵ transforms the system in a strictly hyperbolic one, enabling the use of Riemann solvers, such as the Roe solver [26]. The perturbation parameter is equivalent to a particle pressure [27] with the pressure proportional to the density, $p = a^2\rho$. If the sound speed vanishes, $a \to 0$, then the pressureless system is recovered. [28] applied an idea developed originally in computational magnetohydrodynamics (MHD) [29]. Starting with the Eulerian droplet equation system, they add and subtract a vector term involving the divergence of a particle pressure. Next, they split the system between a strictly hyperbolic part and a source term. They suggest a HLLC approximate Riemann solver that satisfied the positivity condition for the liquid water content. Once the Eulerian droplet equations are converted into a strictly hyperbolic system, one can use any standard Riemann solvers, such as the Roe solver, the HLLC solver or the HLLC-AUSM solver, as recently studied by [30].

Recent works have led to the development of a new Riemann solver[31, 32]. This solver is of the HLLC type and authors derive it from a Lagrangian framework. In this solver, the face flux is divided into two sub-face fluxes. The sub-face fluxes, related to a node, depend not only on the two states next to the sub-face but also on the nodal velocity. This nodal velocity is computed using all states surrounding the node, hence the name multi-dimensional aware flux. In the context of gas dynamics, the multi-point scheme shows good performance in suppressing numerical instabilities like even-odd decoupling and shock instabilities like carbuncles. In the context of pressureless Euler model, classical methods may encounter convergence difficulties in presence of complex turbulent background flows. This could be related to the weaknesses of two-point schemes, possibly due to their lack of multidimensionality [33, 34]. Moreover thanks to the positivity preserving property of our approach, we expect more robustness compared to classic solvers when droplet trajectories will be unaligned with the mesh lines. This paper is a proof of concept of using the multidimensional aware scheme to solve the pressureless Euler model.

This work modifies the Eulerian droplet equations according to Jung and Myong technique [28]. The objective is to investigate a new Godunov type Finite Volume scheme with multidimensional aware Riemann solvers: the multi-point Riemann solver. First, the Eulerian droplet equation system is derived from the force balance over a single droplet and the equations are modified to obtain a hyperbolic system. Second,

the new multi-point Riemann solver is described in the context of gas dynamics. Third, the algorithm used to solve iteratively the pressureless system of equations is detailed. In the numerical section we present a convergence study for a 1D Riemann problem, and, a more advanced 2D test case – a flow around a cylinder. Conclusions are finally drawn.

2. Problem Statement

This work focuses on 2D situations in a Cartesian referential of center $\mathbf{O} = (0,0)^t$ with unit directions $\mathbf{e}_x = (1,0)^t$ and $\mathbf{e}_y = (0,1)^t$, so that any vector position $\mathbf{x}$ is represented as: $\mathbf{x} = (x,y)^t = x\mathbf{e}_x + y\mathbf{e}_y$. Accordingly any velocity vector is given by $\mathbf{u} = (u,v)^t = u\mathbf{e}_x + v\mathbf{e}_y$.

Physically speaking, inside a cloud, the compressible air and small liquid droplets flow around and impact the aircraft parts. Because the liquid water content is small, the effect of the droplets on the airflow is neglected, and, the flow is modelled as a two-phase material with one way coupling. The droplets are considered rigid and mono-dispersed. First the airflow solution, using classical Euler system of equations, is solved, and, $\mathbf{u}_a$ and ρ_a are then known all over the mesh.

In our model the momentum equations compute the velocity components $\mathbf{u} = (u,v)^t$ of spherical droplets of water. As illustrated on Figure 1, the droplets with diameter $d > 0$ and constant density $\rho_w > 0$ are carried by the airflow of density $0 < \rho_a \ll \rho_w$ and viscosity $\mu > 0$. The air velocity $\mathbf{u}_a = (u_a, v_a)^t$ creates a drag force $\mathbf{F}_D$ parallel to the relative velocity vector $\mathbf{u}_a - \mathbf{u}$. The gravity force, arbitrarily pointing downward in the y directon as $\mathbf{g} = (0,-g)^t$, with $g > 0$, also acts on the droplet, such as the buoyancy force $\mathbf{F}_B = (0, \rho\frac{\rho_a}{\rho_w}g)^t$, which could be possibly neglected thanks to the ratio $\frac{\rho_a}{\rho_w} \ll 1$. These forces accelerate the droplet such that it reaches its velocity $\mathbf{u}$ at time t. The Eulerian droplet equations consist of a mass

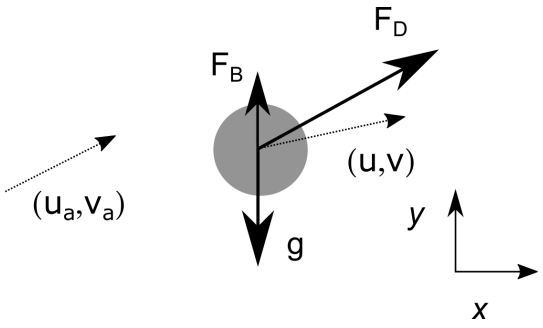

Figure 1: Forces acting on a droplet in an airflow

conservation equation for the liquid water content, ρ, and momentum conservation equations for the droplet velocity $\mathbf{u}$. The momentum equations do include the source terms simulating the drag force exerted by the

air onto the droplets:

$$\mathbf{F}_D = A_u(\mathbf{u}_a - \mathbf{u}), \tag{1}$$

where the coefficient A_u adapted from [13] is defined as

$$A_u = \frac{3}{4}\frac{\rho C_D \mathrm{Re}\mu}{\rho_w d^2} = \frac{3}{4}\rho\frac{\rho_a}{\rho_w}\frac{C_D}{d}\|\mathbf{u}_a - \mathbf{u}\| \geq 0, \tag{2}$$

and the local Reynolds number being defined as $\mathrm{Re} = \dfrac{\rho_a d}{\mu}\|\mathbf{u}_a - \mathbf{u}\|$. At last the droplet drag coefficient C_D is modelled as

$$C_D = \begin{cases} \dfrac{24}{\mathrm{Re}}\left(1.0 + 0.15\mathrm{Re}^{0.687}\right) & \text{if} \quad \mathrm{Re} \leq 1300, \\ 0.4 & \text{if} \quad \mathrm{Re} > 1300. \end{cases} \tag{3}$$

Notice that C_D and $\mathbf{A_u}$ are functions of density and velocity variables. Usually the droplets behave as a pressureless gas, and, unless the calculation requires droplet temperatures, the system does not involve any energy equation.

Consequently the 2D pressureless equations, named here the Eulerian droplet equations, are expressed as

$$\frac{\partial}{\partial t}\mathbf{U} + \nabla \cdot \mathbb{F}(\mathbf{U}) = \mathbf{Q}(\mathbf{U}), \tag{4}$$

and feature the conservative variables, the physical flux and source term as:

$$\mathbf{U} = \begin{pmatrix} \rho \\ \rho\mathbf{u} \end{pmatrix}, \quad \mathbb{F}(\mathbf{U}) = \begin{pmatrix} \rho\mathbf{u}^t \\ \rho\mathbf{u}\otimes\mathbf{u} \end{pmatrix}, \quad \mathbf{Q}(\mathbf{U}) = \begin{pmatrix} 0 \\ A_u(\mathbf{u}_a - \mathbf{u}) + \rho\left(1 - \dfrac{\rho_a}{\rho_w}\right)\mathbf{g} \end{pmatrix} \tag{5}$$

where $\mathbf{F}_D = A_u(\mathbf{u}_a - \mathbf{u})$ stands for the aerodynamic drag force in x and y directions, $\mathbf{F}_B = -\rho\frac{\rho_a}{\rho_w}\mathbf{g}$ is the buoyancy force and $\mathbf{F}_G = \rho\mathbf{g}$ is the gravity force. Notice that the convective part of the Eulerian droplet equations is not strictly hyperbolic. When considering $\mathbf{Q}(\mathbf{U}) = \mathbf{0}$, the homogeneous system has a non-diagonalizable Jacobian matrix with the degenerate eigenvalue u (multiplicity 3). In order to derive weak solutions to these equations, some special treatments are needed. When it comes to writing a Finite Volume (FV) simulation code based on an approximate Riemann Solver (RS), most of the time, a strictly hyperbolic system of equations is required. Therefore, classical RS cannot solve appropriately such a weakly hyperbolic system. Here, to circumvent this problem, the same artificial term on both sides of the equations is added to the system [35]. As such, the modified system turns into a strictly hyperbolic system, and, classical RS within a FV code becomes once again usable.

2.1. Modified pressureless model

One possible modified pressureless model consists in changing system (4) into

$$\frac{\partial}{\partial t}\mathbf{U} + \nabla \cdot \mathbb{F}(\mathbf{U}) = \nabla \cdot \mathbb{F}_p(\mathbf{U}) + \mathbf{Q}(\mathbf{U}), \tag{6}$$

where $\mathbf{U}$ remains unchanged but

$$\mathbb{F}(\mathbf{U}) = \begin{pmatrix} \rho \mathbf{u}^t \\ \rho \mathbf{u} \otimes \mathbf{u} + p\mathbb{I} \end{pmatrix}, \quad \mathbb{F}_p(\mathbf{U}) = \begin{pmatrix} \mathbf{0}^t \\ p\mathbb{I} \end{pmatrix} \quad \mathbf{Q}(\mathbf{U}) = \begin{pmatrix} 0 \\ A_u(\mathbf{u}_a - \mathbf{u}) + \rho\left(1 - \frac{\rho_a}{\rho_w}\right)\mathbf{g} \end{pmatrix}. \tag{7}$$

Notice that the artificial pressure terms in $\mathbb{F}$ and $\mathbb{F}_p$ do annihilate each other. The value of the artificial pressure p relates the liquid water density, ρ, the gravity magnitude, g, and a reference droplet diameter $d > 0$ as

$$p \equiv p(\rho) = \rho g d. \tag{8}$$

The idea is to supplement the system with an artificial pressure term equivalent to a classical pressure, $p \propto \rho$, for continuous compressible fluid. Specifically, for isothermal Euler equations, we have $p(\rho) = a^2\rho$, where a is the speed of sound. Here, for our homogeneous system, if one defines $a = \sqrt{gd}$, then one retrieves the isothermal Euler equations. They are known to be strictly hyperbolic with ordered eigenvalues $u - \sqrt{gd} < u < u + \sqrt{gd}$, supplemented by a full set of right eigenvectors. Consequently, classical RS based on the eigenstructure of the homogeneous system could be employed safely. Obviously, at the price of solving an extra source-term.

2.2. Boundary conditions

At farfield, inlet or outlet supersonic boundary conditions are imposed, taking into account that the speed of sound $a = \sqrt{gd}$ should be small compared to the droplet velocity, recalling that a is linked to the artificial pressure $p = \rho g d$. At any solid surface, a special boundary condition must be imposed. The impinging droplets stay on the surface and no droplet are ejected from the surface. Thus, the flow can leave the computational domain but it cannot enter into it. To emulate such a behavior, one have to first compute the projection of the velocity vector onto the solid surface normal vector, $u_n = \mathbf{u} \cdot \mathbf{n}$. Then, if the flow leaves the computational domain, supersonic outlet boundary conditions are imposed. In the contrary, the flow enters the computational domain, i.e. the droplets are ejected from the wall, a supersonic inlet is imposed

with the conservative variables set to zero. It is summarized as

$$\mathbf{u}_{\text{wall}} = \begin{cases} \mathbf{0} & \text{if} \quad u_n > 0, \\ \mathbf{u} & \text{if} \quad u_n \leq 0. \end{cases} \tag{9}$$

3. Godunov type Finite Volume schemes

In this section we describe a FV discretization to solve the previous Eulerian droplet equations in 2D on unstructured meshes. This numerical method is inspired from the seminal work of G. Gallice [36] which has been recently pursued in [37] in 1D and [31] in 2D. This solver is a particular FV scheme designed for hyperbolic systems of conservation laws, possibly with source terms. A FV scheme considers constant variable per cell, the values of which evolve in time via interface fluxes, which are usually located in-between two cells. Classically, a RS is computed between two constant states in the normal direction to an edge/face between two neighbor cells. Contrarily in the work [31], a subface (half-face) based RS is computed in such a way that all surrounding neighbour cells participate to the update of the current one. Our goal in this work is to adapt this subface-based FV scheme to solve the Eulerian droplet equations.

More precisely this new FV scheme is written in a non-conservative way to allow for discontinuous fluxes across subfaces. Conservation is, however, retrieved by equilibrating the vertex based flux jumps. Although not classic, this approach has the main advantage to couple all neighbour cells regardless the mesh structure or the cell type. The RS, which is of 'HLLC type' [38], is derived from the Lagrangian framework [36] and further expressed in the Eulerian one by a Lagrange-to-Euler mapping. As such the properties of the Lagrangian RD are naturally inherited by the Eulerian one: consistency, positivity preservation, entropy dissipation and wave ordering [31] with a well-defined time-step control. When tested on hydrodynamics equations, this new FV scheme seems relatively insensitive to spurious oscillatory phenomena sometimes encountered such as the carbuncle phenomena, odd-even decoupling, excess wall heating, etc. [39, 40].

In this section we will recall the main characteristics of this new Godunov type FV scheme with multidimensional aware RS. This scheme is referred as the 'Multi-point' solver. We will also point the differences with a classical FV scheme using the HLLC RS which we refer to as a 'two-point' solver.

3.1. Finite Volume framework on unstructured mesh

The 2D computational domain Ω is a polygon covered by non-overlapping polygonal cells ω_c. c is the generic label of any of the $N_c > 0$ cells. $\mathcal{P}(c)$ the set of the points of cell ω_c. The generic label of a point is $1 \leq p \leq N_p$ and $\mathbf{x}_p = (x_p, y_p)^t$ denotes its vector position. The points of the cell ω_c are counter-clockwise ordered, and p^- and p^+ are respectively the previous and the next points with respect to p, see figure 2.

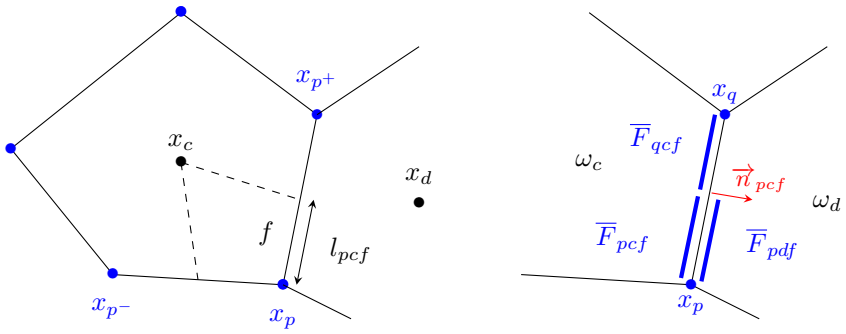

Figure 2: Notation and geometrical entities in a generic cell ω_c — Left: polygonal cell ω_c and subface f associated to subcell ω_{cp} — Right: subface (half interface) between cell ω_c and cell ω_d, with possibly discontinuous fluxes $\overline{F}_{pcf}, \overline{F}_{pdf}$.

The cell center $\mathbf{x}_c = (x_c, y_c)^t$ is the isobarycenter of the points in $\mathcal{P}(c)$. The sub-cell ω_{pc} is the quadrangle formed by joining the cell center, $\mathbf{x}_c$, to the midpoints of the edges $[\mathbf{x}_{p^-}, \mathbf{x}_p]$, $[\mathbf{x}_p, \mathbf{x}_{p^+}]$ and to the vertex $\mathbf{x}_p$. The set of sub-cells ω_{pc} for $p \in \mathcal{P}(c)$ constitutes a partition of the cell ω_c, that is, $\omega_c = \bigcup_{p\in\mathcal{P}(c)} \omega_{pc}$. We can define the dual volume around point p as: $\omega_p = \bigcup_{c\in\mathcal{C}(p)} \omega_{pc}$, where $\mathcal{C}(p)$ is the set of cells surrounding point p. The set of faces/edges of the cell ω_c is denoted by $\mathcal{F}(c)$. Each face f of cell ω_c is decomposed into subfaces (half-faces) by means of the partition of c induced by the sub-cells pc for $p \in \mathcal{P}(c)$. Doing so, we define $\mathcal{SF}(pc)$ the set of subfaces attached to the sub-cell ω_{pc}. We denote respectively by l_{pcf} and $\mathbf{n}_{pcf} = (n_{x,pcf}, n_{y,pcf})^t$ the length and the unit outward-pointing normal of the subface f of cell c attached to point p. Sometimes we lighten the notation to l_f and $\mathbf{n}_f = (n_{x,f}, n_{y,f})^t$. We observe that the set of subfaces $\mathcal{SF}(pc)$ for $p \in \mathcal{P}(c)$ constitutes a partition of the set of faces of ω_c, that is, $\mathcal{F}(c) = \bigcup_{p\in\mathcal{P}(c)} \mathcal{SF}(pc)$. Given a cell c and one of its faces f, the unique 'neighbour' cell associated is $d(c, f)$ or simply d to shorten the notation. The set of neighbours of the cell c is called $\mathcal{N}(c)$ and it will be more appropriately defined, either faced-based or node-based.

Any vector $\mathbf{a}$ can be projected onto the canonical or normal/tangent $\mathbf{n}_f \perp \mathbf{t}_f$ base associated to a generic face f as: $\mathbf{a} = a_\mathbf{n}\mathbf{n}_f + a_\mathbf{t}\mathbf{t}_f$.

The time domain $[0, t_{\text{final}}]$ with $t_{\text{final}} > 0$ is split into time intervals $[t^n, t^{n+1}]$ with time-step $\Delta t > 0$ such that $t^{n+1} = t^n + \Delta t$. Δt shall be constrained by stability and positivity arguments.

The mean value of a vector $\mathbf{U}$ in cell ω_c at time t, and t^n is denoted as

$$\mathbf{U}_c(t) \equiv \frac{1}{|\omega_c|}\int_{\omega_c} \mathbf{U}(\mathbf{x}, t)\, dv, \qquad \mathbf{U}_c^n = \mathbf{U}_c(t^n) \equiv \frac{1}{|\omega_c|}\int_{\omega_c} \mathbf{U}(\mathbf{x}, t^n)\, dv, \tag{10}$$

where $|\omega_c|$ is the surface of cell ω_c.

3.2. Subface-based FV scheme for 2D isothermal gasdynamics

Let us consider the 2D isothermal Euler equations with the equation of state $p = K\rho^\gamma$ with $K = gd > 0$, a constant, and, $\gamma = 1$, for which the sound speed is given by $a^2 = K$. Doing this, the considered model consists of the homogeneous system (6) which is further integrated over a generic cell ω_c and time interval $[t^n, t^{n+1}]$ as

$$\int_{t^n}^{t^{n+1}} \int_{\omega_c} \left(\frac{\partial}{\partial t} \mathbf{U}(\mathbf{x}, t) + \nabla \cdot \mathbb{F}(\mathbf{U}(\mathbf{x}, t)) \right) dv\, dt = \mathbf{0}. \tag{11}$$

Considering (10) we can rewrite (11) as

$$\mathbf{U}_c^{n+1} - \mathbf{U}_c^n + \frac{1}{|\omega_c|} \int_{t^n}^{t^{n+1}} \int_{\partial\omega_c} \mathbb{F}(\mathbf{U}(\mathbf{x}, t))\mathbf{n}\, ds\, dt = \mathbf{0}. \tag{12}$$

Notice that in (12) no approximation has yet been made. An explicit version of (12) consists in approximating the time integral at discrete time t^n as

$$\mathbf{U}_c^{n+1} - \mathbf{U}_c^n + \frac{\Delta t}{|\omega_c|} \int_{\partial\omega_c} \mathbb{F}(\mathbf{U}^n)\mathbf{n}\, ds = \mathbf{0}. \tag{13}$$

The FV scheme (13) requires the construction of an approximation of the explicit normal flux integral. Following [31] we design an original node-based approximation of this integral term relying on the partition of ω_c into sub-cells ω_{pc}, and subfaces of subcells, as

$$\int_{\partial\omega_c} \mathbb{F}(\mathbf{U}^n)\mathbf{n}\, ds = \sum_{p\in\mathcal{P}(c)} \int_{\partial\omega_{pc}\cap\partial\omega_c} \mathbb{F}(\mathbf{U}^n)\mathbf{n}\, ds \simeq \sum_{p\in\mathcal{P}(c)} \sum_{f\in\mathcal{SF}(pc)} l_{pcf}\overline{\mathbf{F}}_{pcf}. \tag{14}$$

where the surface integral term in the middle term is approximated along the subfaces f by means of the subface flux attached to the subcell pc which is denoted by $\overline{\mathbf{F}}_{pcf}$.
Substituting (14) into (13) yields the subface-based generic Finite Volume scheme

$$\mathbf{U}_c^{n+1} - \mathbf{U}_c^n + \frac{\Delta t}{|\omega_c|} \sum_{p\in\mathcal{P}(c)} \sum_{f\in\mathcal{SF}(pc)} l_{pcf}\overline{\mathbf{F}}_{pcf} = \mathbf{0}, \tag{15}$$

entirely characterized by the subface flux $\overline{\mathbf{F}}_{pcf}$.

Remark 1. *We can retrieve the classical face-based FV scheme (also called two-point FV scheme)*

$$\mathbf{U}_c^{n+1} - \mathbf{U}_c^n + \frac{\Delta t}{|\omega_c|} \sum_{f\in\mathcal{F}(c)} l_f\overline{\mathbf{F}}_f = \mathbf{0}, \tag{16}$$

assuming that the face flux, $l_f\overline{\mathbf{F}}_f$, from face $f = [\boldsymbol{x}_p, \boldsymbol{x}_q]$ is equal to the sum of the two subface fluxes, that is

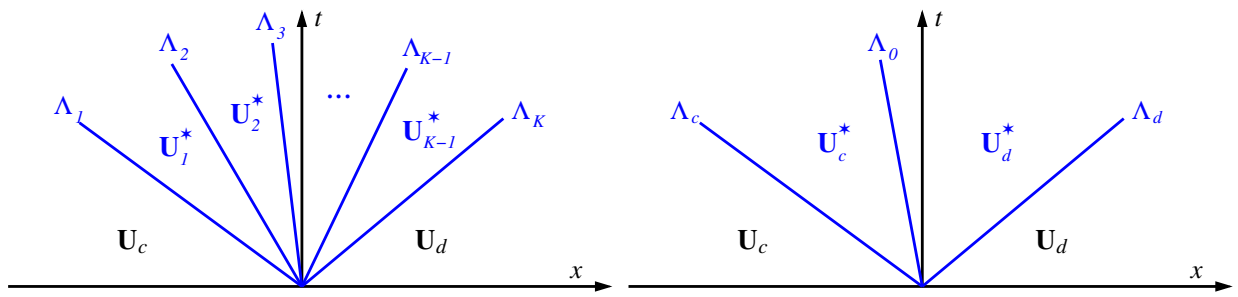

Figure 3: Left: illustration of a generic simple Riemann solver — Right: simple Riemann problem for our system composed of three waves and two intermediate states.

$$l_f \overline{\mathbf{F}}_f = l_{pcf} \overline{\mathbf{F}}_{pcf} + l_{qcf} \overline{\mathbf{F}}_{qcf}.$$

3.2.1. Simple Lagrangian/Eulerian Riemann Solvers

A RS consists in computing, exactly or approximately, the solution of the system in the normal direction $\mathbf{n}$ to an edge separating two constant cell states $\mathbf{U}_c$ and $\mathbf{U}_d$. A so-called simple Eulerian RS considers constant intermediate states $\mathbf{U}_k^\star$, separated by simple waves, therefore given by constant wave speeds Λ_k, for $k = 1, \ldots, K$, with $\mathbf{U}_0^\star = \mathbf{U}_c$ and $\mathbf{U}_K^\star = \mathbf{U}_d$, see figure 3 for an illustration. In our case we choose a simple RS made of two intermediate states $\mathbf{U}_c^\star$ and $\mathbf{U}_d^\star$, and, three waves Λ_c, Λ_0 and Λ_d. These waves are deduced from their Lagrangian counterparts $-\lambda_c \leq \lambda_0 = 0 \leq \lambda_d$ as

$$\Lambda_c = u_{\mathbf{n},c} - \lambda_c \frac{1}{\rho_c} = u_{\mathbf{n}}^\star - \lambda_c \frac{1}{\rho_c^\star}, \quad \Lambda_0 = u_{\mathbf{n}}^\star, \quad \Lambda_d = u_{\mathbf{n}}^\star + \lambda_d \frac{1}{\rho_d^\star} = u_{\mathbf{n},d} + \lambda_d \frac{1}{\rho_d}. \tag{17}$$

In (17) we have considered the projection of the velocity vectors onto the normal, such that $u_{\mathbf{n},c} = \mathbf{u}_c \cdot \mathbf{n}$ and $u_{\mathbf{n},d} = \mathbf{u}_d \cdot \mathbf{n}$. Also, $u_{\mathbf{n}}^\star = \mathbf{u}_p \cdot \mathbf{n}$ is the projection of an unknown point-centered velocity vector $\mathbf{u}_p$.
If the RS preserves the positivity of intermediate densities, *i.e.*: $\rho_c^\star \geq 0$ and $\rho_d^\star \geq 0$, then the Eulerian wave speeds in (17) are ordered by construction: $\Lambda_c \leq \Lambda_0 \leq \Lambda_d$. In [31], it is shown that the positivity holds true granted that the Lagrangian wave speeds satisfy an explicit condition on the star velocity $u_{\mathbf{n}}^\star$. The Lagrangian and Eulerian simple approximate RSs operating over the two states, called left and right, and respectively associated to the cell c and d in the direction $\mathbf{n}$, are expressed as (m is the constant Lagrangian

mass)

$$\mathbf{W}_L\left(\mathbf{V}_c,\mathbf{V}_d,\frac{m}{t}\right)=\begin{cases}\mathbf{V}_c \ \text{ if } \frac{m}{t}\leq-\lambda_c,\\ \mathbf{V}_c^\star \ \text{ if } -\lambda_c<\frac{m}{t}\leq 0,\\ \mathbf{V}_d^\star \ \text{ if } 0<\frac{m}{t}\leq\lambda_d,\\ \mathbf{V}_d \ \text{ if } \lambda_d<\frac{m}{t}.\end{cases}\quad \mathbf{W}_E\left(\mathbf{U}_c,\mathbf{U}_d,\frac{x_{\mathbf{n}}}{t}\right)=\begin{cases}\mathbf{U}_c & \text{if } \frac{x_{\mathbf{n}}}{t}\leq\Lambda_c,\\ \mathbf{U}_c^\star=\mathbf{U}(\mathbf{V}_c^\star) & \text{if } \Lambda_c<\frac{x_{\mathbf{n}}}{t}\leq\Lambda_0,\\ \mathbf{U}_d^\star=\mathbf{U}(\mathbf{V}_d^\star) & \text{if } \Lambda_0<\frac{x_{\mathbf{n}}}{t}\leq\Lambda_d,\\ \mathbf{U}_d & \text{if } \Lambda_d<\frac{x_{\mathbf{n}}}{t}.\end{cases} \tag{18}$$

Here, $\mathbf{V}\mapsto\mathbf{U}(\mathbf{V})$ is the Lagrange-to-Euler mapping defined by $\mathbf{V}=\frac{1}{\rho}(\mathbf{U}-\rho\mathbf{e}_x)+\frac{1}{\rho}\mathbf{e}_x$, where $\mathbf{e}_x=(1,0)^t$ [36, 31]. Because the Eulerian variables are $\mathbf{U}=(\rho,\rho u_{\mathbf{n}},\rho u_{\mathbf{t}})^t$, then the Lagrangian ones are $\mathbf{V}=(\rho,u_{\mathbf{n}},u_{\mathbf{t}})^t$. The Eulerian intermediate states, $\mathbf{U}_s^\star=(\rho_s^\star,\rho_s^\star u_{\mathbf{n}}^\star,\rho_s^\star u_{\mathbf{t},s}^\star)^t$, will be entirely deduced from their Lagrangian counterparts, $\mathbf{V}_s^\star=(1/\rho_s^\star,u_{\mathbf{n}}^\star,u_{\mathbf{t},s}^\star)^t$ for $s=c,d$ respectively, refer to [36, 31] for more details. Following the derivation in [31], we observe that the simple Lagrangian RS $\mathbf{W}_L$ in (18) is parameterized by the normal star-velocity $u_{\mathbf{n}}^\star$, and, the intermediate states then read

$$\frac{1}{\rho_c^\star}=\frac{1}{\rho_c}+\frac{u_{\mathbf{n}}^\star-u_{\mathbf{n},c}}{\lambda_c},\qquad \frac{1}{\rho_d^\star}=\frac{1}{\rho_d}-\frac{u_{\mathbf{n}}^\star-u_{\mathbf{n},d}}{\lambda_d}, \tag{19}$$

$$u_{\mathbf{t},c}^\star=u_{\mathbf{t},c},\qquad u_{\mathbf{t},d}^\star=u_{\mathbf{t},d}. \tag{20}$$

In the Rankine-Hugoniot jump conditions (19-20) we have ommitted the ones related to the normal velocity which state that

$$\lambda_c(u_{\mathbf{n}}^\star-u_{\mathbf{n},c})+(\overline{p}_c-p_c)=0,\quad \text{and}\quad \lambda_d(u_{\mathbf{n}}^\star-u_{\mathbf{n},d})-(\overline{p}_d-p_d)=0, \tag{21}$$

where $\overline{p}_c$ and $\overline{p}_d$ may be different. Next, we invoke the consistency of the simple Lagrangian RS. By arranging the previous equations, we arrive at

$$\overline{p}_d-\overline{p}_c=(\lambda_c+\lambda_d)u_{\mathbf{n}}^\star-\lambda_c u_{\mathbf{n},c}-\lambda_d u_{\mathbf{n},d}+p_d-p_c=(\lambda_c+\lambda_d)\left\{u_{\mathbf{n}}^\star-\left[\frac{\lambda_c u_{\mathbf{n},c}+\lambda_d u_{\mathbf{n},d}}{\lambda_c+\lambda_d}-\frac{p_d-p_c}{\lambda_c+\lambda_d}\right]\right\}. \tag{22}$$

Introducing the Godunov acoustic normal velocity

$$\overline{u}_{\mathbf{n}}=\frac{\lambda_c u_{\mathbf{n},c}+\lambda_d u_{\mathbf{n},d}}{\lambda_c+\lambda_d}-\frac{p_d-p_c}{\lambda_c+\lambda_d}, \tag{23}$$

we can rewrite (22) as

$$\overline{p}_d-\overline{p}_c=(\lambda_c+\lambda_d)\left\{u_{\mathbf{n}}^\star-\overline{u}_{\mathbf{n}}\right\}. \tag{24}$$

It is then important to remark that if $u^\star_{\mathbf{n}} = \overline{u}_{\mathbf{n}}$ then $\overline{p}_d = \overline{p}_c$ and the simple Lagrangian RS is consistent with its underlying conservation law. Thus, it induces a classical conservative Godunov-type FV scheme. On the other hand, if $u^\star_{\mathbf{n}} \neq \overline{u}_{\mathbf{n}}$, then the simple Lagrangian RS is not consistent with its underlying conservation law and thus does not induce a conservative Godunov-type FV scheme. The next section will construct a nodal solver that allows to retrieve a node-based conservation.

The Lagrangian wave speeds $-\lambda_c$, λ_0 and λ_d are ordered by construction and must be large enough to ensure positivity preservation, for instance by fulfilling [31]

$$\lambda_c \geq \max\left(\rho_c a_c, -\rho_c(u^\star_{\mathbf{n}} - u_{\mathbf{n},c})\right), \quad \lambda_d \geq \max\left(\rho_d a_d, \rho_d(u^\star_{\mathbf{n}} - u_{\mathbf{n},d})\right). \tag{25}$$

Notice that the simple RS has been parametrized by the only remaining unknown: $u^\star_{\mathbf{n}}$. Also, by construction, the Eulerian approximate RS $\mathbf{W}_E$ inherits the same properties as its Lagrangian counterpart $\mathbf{W}_L$ such as positivity preservation, wave ordering, etc.

3.2.2. Nodal solver

Recall that the simple Lagrangian RS previously described is parametrized by the normal velocity $u^\star_{\mathbf{n}}$ to the current subface. Consequently, around a point p, there is as many normal velocities as subfaces impinging on p. We make the fundamental assumption that there exists a unique nodal velocity $\mathbf{u}_p$ such that for any point p we have

$$\mathbf{u}_p \cdot \mathbf{n}_f = u^\star_{\mathbf{n}_f}, \quad \forall f \in \mathcal{SF}(p), \tag{26}$$

that is for any subface f impinging at the node p with normal $\mathbf{n}_f$. Therefore $\mathbf{u}_p$ is shared by all subfaces/cells around p, see figure 4. We recall that f is one subface impinging at point p which shares cell c and d, the subface normal is $\mathbf{n}_f$ and is oriented from c to d, and l_f is the half-length of the subface f. The nodal solver consists in solving a balance equation around the point p by summing the contributions produced by each RS.

$$\sum_{f\mathcal{SF}(p)} l_f(\overline{p}_d - \overline{p}_c)\mathbf{n}_f = \mathbf{0}. \tag{27}$$

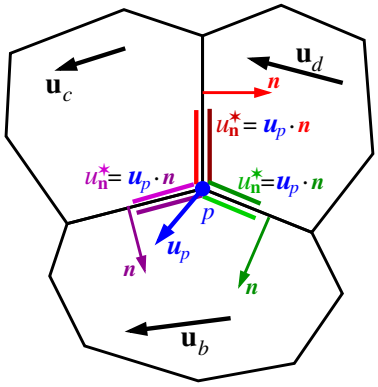

Figure 4: Illustration of the situation around a point p sharing three cells. The nodal velocity $\mathbf{u}_p$ projected onto the subface normals $\mathbf{n}$ producing the $u^\star_{\mathbf{n}}$ velocities that parametrize the Riemann solver in direction $\mathbf{n}$.

Substituting (24) into (28) and reminding that $u^\star_{\mathbf{n}} = \mathbf{u}_p \cdot \mathbf{n}_f$, yields the linear system

$$\sum_{f \mathcal{SF}(p)} l_f \left((\lambda_c + \lambda_d) \left\{ \mathbf{u}_p \cdot \mathbf{n}_f - \overline{u}_{\mathbf{n}} \right\} \right) \mathbf{n}_f = \mathbf{0} \tag{28}$$

$$\iff \underbrace{\left(\sum_{f \mathcal{SF}(p)} l_f (\lambda_c + \lambda_d) \left(\mathbf{n}_f \otimes \mathbf{n}_f \right) \right)}_{\mathbb{M}_p} \mathbf{u}_p = \underbrace{\sum_{f \mathcal{SF}(p)} l_f (\lambda_c + \lambda_d) \overline{u}_{\mathbf{n}} \mathbf{n}_f}_{\mathbf{w}_p}, \tag{29}$$

where $(\mathbf{n}_f \otimes \mathbf{n}_f) = \begin{pmatrix} n_x^2 & n_x n_y \\ n_x n_y & n_y^2 \end{pmatrix}$ is a 2×2 matrix in 2D attached to subface f. The matrix $\mathbb{M}_p$ is always invertible if the mesh is non-degenerated. This linear system has a unique nodal velocity vector solution $\mathbf{u}_p$ for any point p.

Once $\mathbf{u}_p$ is known, we can compute $u^\star_{\mathbf{n}_f}$, the Lagrangian wave speeds λ, then the intermediate Lagrangian Riemann states $\mathbf{V}^*_s$, and, finally, deduce the Eulerian ones $\mathbf{U}^*_s$. The foregoing system has been already obtained when constructing a cell-centered FV discretization of multidimensional Lagrangian hydrodynamics [41], also retrieved in [42, 31] for designing an Eulerian FV scheme.

By construction, the Eulerian approximate RS $\mathbf{W}_E$ inherits the same properties as its Lagrangian counterpart $\mathbf{W}_L$ such as the positivity preservation, entropy production and wave ordering [31].

3.2.3. Multi-dimensional aware numerical flux.

Recall that the subface-based generic FV scheme (15) is entirely characterized by the subface flux $\overline{\mathbf{F}}_{pcf}$, which is computed taking into account the Eulerian RS (derived from its Lagrangian counterpart). Hence,

the subface flux $\overline{\mathbf{F}}_{pcf}$ between cells c and d sharing point p in direction $\mathbf{n} = \mathbf{n}_{pcf}$ is given by:

$$\begin{aligned}\overline{\mathbf{F}}_{\mathbf{n}} = \frac{1}{2}\left[\mathbf{F}_{\mathbf{n}}(\mathbf{U}_c) + \mathbf{F}_{\mathbf{n}}(\mathbf{U}_d)\right] &- \frac{1}{2}\Big[|\Lambda_c|(\mathbf{U}_c^\star - \mathbf{U}_c) + |\Lambda_0|(\mathbf{U}_d^\star - \mathbf{U}_c^\star) + |\Lambda_d|(\mathbf{U}_d - \mathbf{U}_d^\star)\Big] \\ &- \frac{\lambda_c + \lambda_d}{2}\left[\mathbf{u}_p \cdot \mathbf{n} - \overline{u}_{\mathbf{n}}\right](0,1,0)^t, \end{aligned} \tag{30}$$

where the point velocity $\mathbf{u}_p$ is computed by the nodal solver, the Eulerian wave speeds by (17), while the Lagrangian ones (25) and the Godunov acoustic mean velocity $\overline{u}_{\mathbf{n}_{pcf}}$ is given by (23). The extra-term in (30) only appears for the momentum in the normal direction. It is easy to recognize that a classical (two points) numerical flux is retrieved when one set $\mathbf{u}_p \cdot \mathbf{n} = \overline{u}_{\mathbf{n}}$ because the last term in (30) cancels out. In this only case, the flux is the same at the face f for cell c and d but applied with a plus (resp. a minus) sign in the cell c (resp. d). The conservation is classically obtained because there is no flux jump at the interface between neighbour cells. However there is no reason *a priori* that a unique nodal velocity $\mathbf{u}_p$ exists to fulfill this requirement.

Contrarily, in our approach, we accept that $\mathbf{u}_p \cdot \mathbf{n} \neq \overline{u}_{\mathbf{n}}$. As such the numerical flux depends not only on the two states adjacent to the subface but also on all states surrounding node p through the expression of the nodal velocity $\mathbf{u}_p$. Hence the name multi-point or multidimensional aware flux.

3.3. Time-step condition.

The time step, Δt, is computed to ensure that the updated cell-average value, $\mathbf{U}_c^{n+1}$ is a convex combination of $\mathbf{U}_c^n$, $\mathbf{U}_c^\star$. Omitting the details that can be retrieved in [31] the practical explicit time step condition writes

$$\Delta t_c \leq \frac{|\omega_c|}{\displaystyle\sum_{p\in\mathcal{P}(c)}\sum_{f\in\mathcal{SF}(pc)} l_{pcf}\left(|\mathbf{u}_c^n \cdot \mathbf{n}_{pcf}| + \frac{\lambda_c}{\rho_c^n}\right)}. \tag{31}$$

The minimal time step over the cells is selected and reduced by a CFL < 1 number as

$$\Delta t = \mathrm{CFL}\min_c \Delta t_c \tag{32}$$

3.4. Second-order extension.

The second-order extension of the previous FV scheme is obtained by piece-wise reconstruction of primitive variables supplemented with minmod or Ventakakrishnan slope limiters in space and Strong Stability Preserving Runge-Kutta scheme in time for the second-order extension for the Eulerian FV scheme. The first-order and second-order versions of the scheme have been validated for gas dynamics [37, 31] and shallow water equations [43], in 1D, 2D and 3D.

4. Algorithm for pressureless system of equations

In order to solve the pressureless system of equations, one must adapt the previous solver. The source terms in (7) are easily taken into account. The second and third components of $\int_{\omega_c} \nabla \cdot \mathbb{F}_p(\mathbf{U})\, dv$ are simply discretized as

$$\int_{\partial\omega_c} p\mathbf{n}\, ds = \sum_{f\in\mathcal{F}(c)} l_f p_f \mathbf{n}_f, \tag{33}$$

where $p_f = (\rho_f)gd$, and, ρ_f is given by the Riemann solver, that is, it is either ρ_L, $\rho_L^\star$, $\rho_R^\star$ or ρ_R depending on the wave speeds, see (18).

On the other hand $\mathbf{Q}$ is nothing but a reaction term which at first and second orders in space can be approximated as

$$\int_{\omega_c} \mathbf{Q}(\mathbf{U})\, dv = |\omega_c| \begin{pmatrix} 0 \\ (A_u)_c\left((u_a)_c - u_c^n\right) \\ (A_u)_c\left((v_a)_c - v_c^n\right) - \rho_c^n g(1-(\rho_a)_c/\rho_w) \end{pmatrix}. \tag{34}$$

For the second order in time, the source terms are approximated once for the predictor and one more time for the corrector stage (the same if a RK scheme is employed).
This completes the description of the numerical method.

5. Numerical results

In this section, we present two test cases to present the behavior of the numerical method. The first one is a classical Riemann problem for which we perform a grid convergence study. Then a more advanced 2D test involving the flow around a cylinder is simulated for which we show that the current numerical method is able to produce a physically valid solution. Notice that this numerical method has been already validated for gas dynamics and shallow-water systems of equations [31, 43]. The Courant number is set to 0.5 for all computations.

5.1. 1D Riemann problem

The first test case is a 1D Riemann problem on domain $[0:50]$ where the discontinuity is located at $x = 25$. The left/right states have the same density of 1 kg/m^{-3}, and $v = 0$ component. The x-velocity component are $u_L = -5$ m/s and $u_R = 5$ m/s. This leads to the generation of two rarefaction waves

emanating from the discontinuity, leading to an almost vaccum central state. The parameters are set to $g = 1$ and $d = 1$ for simplification. For this test the source term is canceled to solely validate the numerical method for the homogeneous system of PDEs. In figure 5 we plot the density/velocity when using a mesh made of 50, 100 and 200 cells. We can clearly see that the method can capture the rarefaction waves and converges as the mesh is further refined. No spurious effect is observed even if the density drops to $\sim 10^{-3}$ in the rarefied central region.

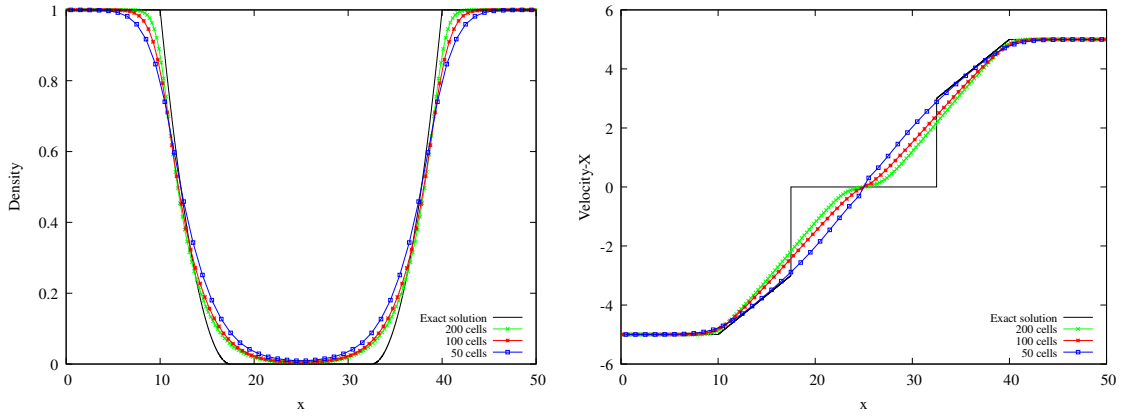

Figure 5: 1D Riemann problem — Numerical density (left) and velocity (right) for 50, 100 and 200 uniform cells.

5.2. Droplets motion around a cylinder

The flow of cloud droplets around a cylinder is studied to demonstrate the new solver's capability. The

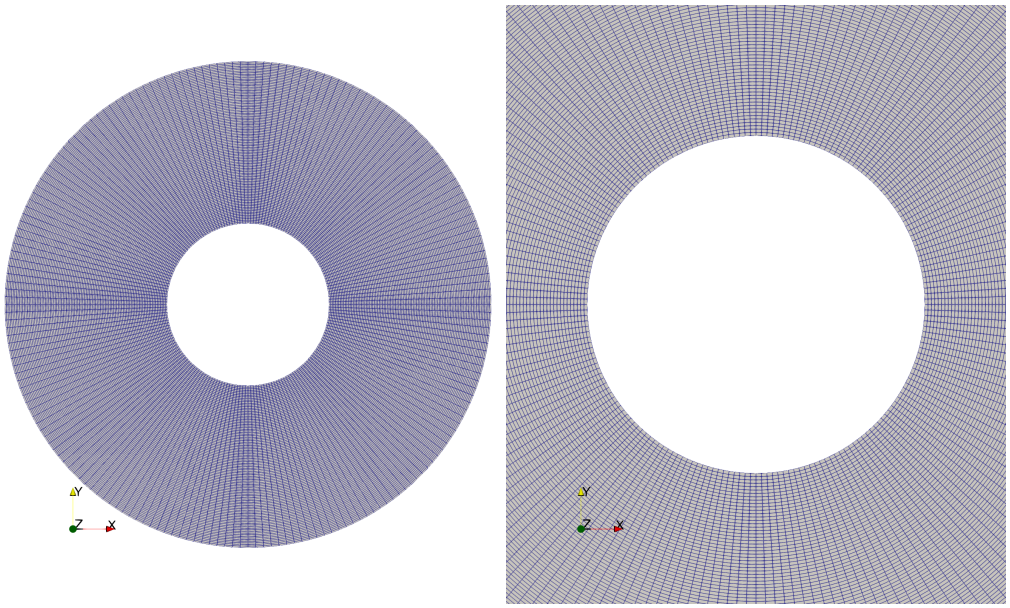

Figure 6: Mesh made of 20000 radial quadrangles. Left: full view. Right: zoom.

computational domain is a disk of radius 1.5 into which a cylinder at position $(0, 0)$ of radius 0.5 is embeded. A structured mesh made of 20000 radial quadrangles is considered – 200 points cover the cylinder and 100 cells in radial direction, see figure 6.

First, the Euler flow solution around this cylinder is computed, see figure 7-top panels. Farfield boundary conditions are imposed on the domain and slip wall boundary condition on the cylinder. The farfield temperature is set to 273.15 K, the pressure at 101325.0 Pa, $u_\infty = 66.2643$ m/s, $\rho_\infty = 1.2922$ kg/m^3 and the Mach number at 0.2.

Once the airflow steady state solution is computed, the pressureless system is solved. The initial velocity field for the droplet is the same as the air velocity field. The water density is $\rho_w = 1000$ kg/m^3. At farfield, the droplet velocity is equal to the air velocity and $\rho/LWC = 1$ with LWC the liquid water content of the cloud. In our computations the reference droplet diameter that appears in the artificial pressure is equal to the droplet diameter and set to 20 μm or 40μm. The steady state solution of the pressureless model is computed and presented in figure 7-middle/bottom. The droplet solution shows an increase in liquid water content on the cylinder front part. Also, very low-density region is visible on the back of the cylinder. In a narrow area close to the cylinder, the liquid water content goes from around one to around zero. Results are in agreement with literature. When the droplet diameter increases from 20 to 40 we can observe a slight variation on the density and velocity component plots. Moreover the heavier the droplets, the less prone they are to be dragged by the background flow, i.e the density of droplets sticking to the cylinder is then higher.

Next in figure 8 we present the streamlines of the background flow, and the solution for droplet diameters 20 and 40 μm. We can obviously observe that the droplet diameter plays a role in the streamlines. The massive droplets are less entrained by the background flow as can be seen on the middle and right panels.

At last, in figure 9, we present the value of the collection efficiency, $\beta_c = \rho_c \max(\mathbf{u}_c \cdot \mathbf{n}_{cf,\text{cyl}}, 0)/u_\infty$, for each cell in contact with the cylinder and where $\mathbf{n}_{f,\text{cyl}}$ is the unit edge normal pointing inside the cylinder. In this figure β_c has been clipped if its value is negative. As expected the maximal values of β are located close to the stagnation point. We can observe that if the droplets are heavier, as expected, the value of β is higer, meaning that more droplets impact the cylinder.

6. Conclusion and Perspectives

In this work, we investigate the multi-point Riemann solver adapted to solve water droplets flow. The two-phase flow is modelled using a one-way coupling. The obtained Eulerian droplet equations, a pressureless equation system, must be modified to obtain a hyperbolic system. A perturbation parameter equivalent to

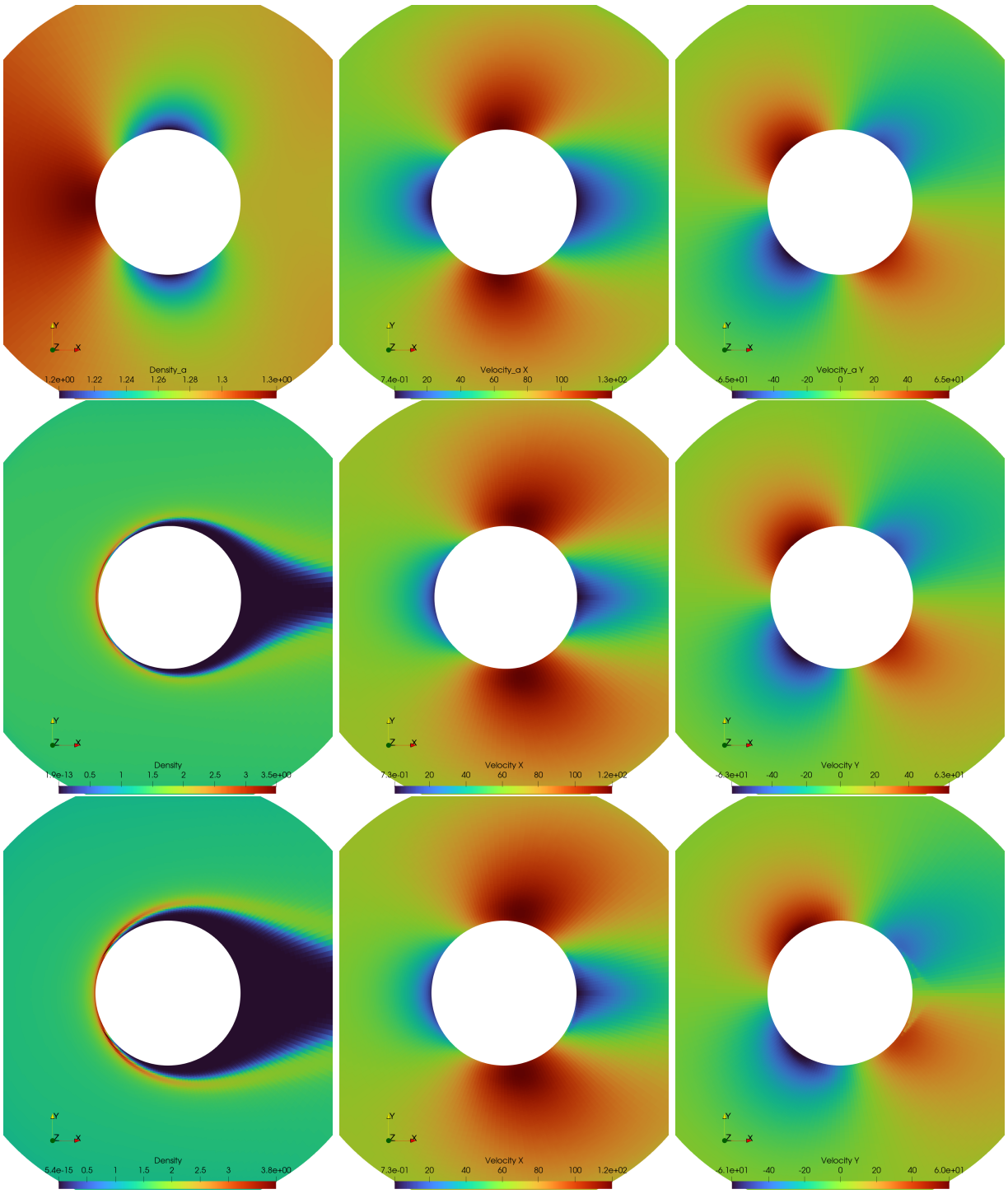

Figure 7: Flow solution around the cylinder. Density, velocity components (letf to right) — Top panels: background flow. Middle/Bottom Panels: pressureless model for droplet diameter of $20\mu m$ and $40\mu m$ respectively.

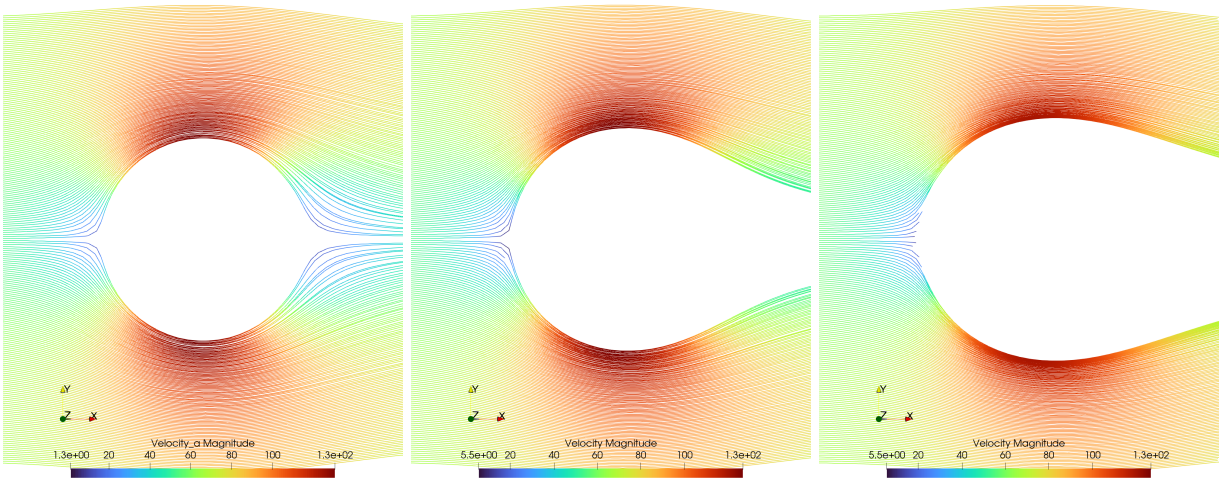

Figure 8: Flow solution around the cylinder. Streamlines of the background flow (left), and of the droplets with diameters 20 μm (center) and 40 μm (right).

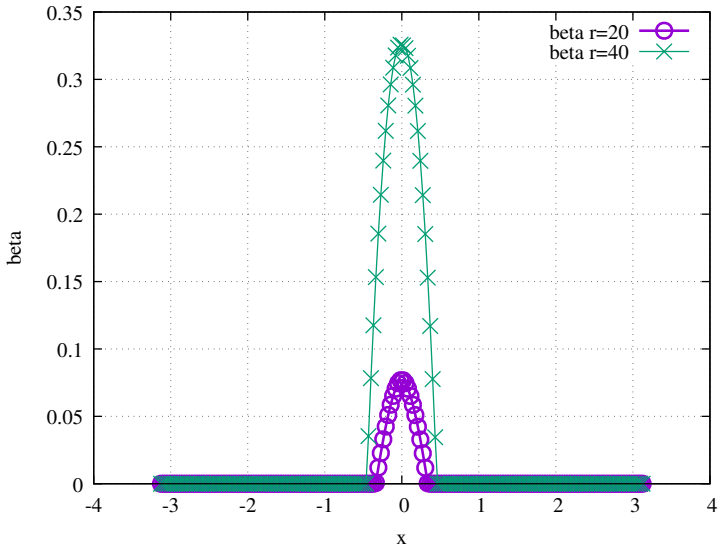

Figure 9: Pressureless flow solution around the cylinder. Collection efficiency $\beta_c = \rho_c \max(\mathbf{u}_c \cdot \mathbf{n}_{cf,\mathrm{cyl}}, 0)/u_\infty$ for droplet diameters 20 μm and 40 μm.

a pressure term is added on the left side and subtracted on the right side of the momentum equations. The multi-point solver is then adapted to the pressureless system. A second order in time explicit scheme is used to march the solution toward the steady state. Preliminary results have been obtained for the simulation of droplets of different masses dragged around a cylinder. This numerical method presents some advantages compared to classical two-point schemes. First it is a mutli-dimensionally aware scheme, meaning that all surrounding cells participate to the update. As such the method is insensitive to classical pathologies that plague classical approaches such as carbuncle or odd-even instabilities. Second, the formulation of the method is by construction independent of the mesh, should it be structured or unstructured, and is positivity and entropy preserving. Therefore there is less mesh-imprint [31, 32]. And third, the derivation of the scheme allows to discretize naturally diffusive terms and effects, see [44, 45], opening the path towards more advanced droplet models. Further investigations and simulations should be performed to assess the capacities of the proposed scheme to solve the pressureless system in genuine demanding flying situations. This is the topic of a set of future works, where genuine comparisons with existing experimental and simulation data are envisionned.

References

[1] P. Appiah-Kubi, B. Martos, I. Atuahene, S. William, U.S. inflight icing accidents and incidents, 2006 to 2010, in: IIE Annual Conference and Expo 2013, 2013.

[2] M. B. Bragg, A. P. Broeren, L. A. Blumenthal, Iced-airfoil aerodynamics, Progress in Aerospace Sciences 41 (2005) 323–362.

[3] Transportation Safety Board of Canada, Air Transportation Safety Investigation Report A17C0146, Report, Transportation Safety Board of Canada (October 2021).

[4] J. Mason, J. Strapp, P. Chow, The ice particle threat to engines in flight, Report AIAA-2006-206, American Institute of Aeronautics and Astronautics (2006).

[5] P. V. Joseph, C. J. Philip, Modeling commercial turbofan engine icing risk with ice crystal ingestion, Tech. Rep. AIAA-2013-2679, American Institute of Aeronautics and Astronautics (2013).

[6] S. K. Thomas, R. P. Cassoni, C. D. MacArthur, Aircraft anti-icing and de-icing techniques and modeling, Journal of Aircraft 33 (5) (1996) 841–854.

[7] R. Hannat, J. Weiss, F. Garnier, F. Morency, Application of the dual kriging method for the design of a hot-air-based aircraft wing anti- icing system, Engineering Applications of Computational Fluid Mechanics 8 (4) (2014) 530–548.

[8] P. McComber, G. Touzot, Calculation of the impingement of cloud droplets in a cylinder by the finite-element method, Journal of the Atmospheric Sciences 38 (1981) 1027–1036.

[9] W. G. Bourgault, Y.and Habashi, J. Dompierre, G. S. Baruzzi, A finite element method study of eulerian droplets impingement models, International Journal of Numerical Methods in Fluids 29 (1999) 429–449. doi:https://doi.org/10.1002/(SICI)1097-0363(19990228)29:4<429::AID-FLD795>3.0.CO;2-F.

[10] C. T. Crowe, Review—numerical models for dilute gas-particle flows, Journal of Fluids Engineering 104 (3) (1982) 297–303. doi:https://doi.org/10.1115/1.3241835.

[11] A. Kulyakhtin, O. Shipilova, M. Muskulus, Numerical simulation of droplet impingement and flow around a cylinder using rans and les models, Journal of Fluids and Structures 48 (2014) 280–294. doi:https://doi.org/10.1016/j.jfluidstructs.2014.03.007.
URL https://www.sciencedirect.com/science/article/pii/S0889974614000541

[12] L. Bennani, P. Trontin, R. Chauvin, P. Villedieu, A non-overlapping optimized schwarz method for the heat equation with non linear boundary conditions and with applications to de-icing, Computers and Mathematics with Applications 80 (6) (2020) 1500–1522. doi:https://doi.org/10.1016/j.camwa.2020.07.017.
URL https://www.sciencedirect.com/science/article/pii/S0898122120302832

[13] R. Clift, J. R. Grace, Weber, Bubbles, Drops, and Particles, Dover Publications, 2005.

[14] W. B. Wright, Validation results for lewice 3.0, Report AIAA Paper 2005-1243, American Institute of Aeronautics and Astronautics Inc. (January 10 - January 13 2005).

[15] T. Hedde, D. Guffond, Onera three-dimensional icing model, AIAA journal 33 (6) (1995) 1038–1045.

[16] F. Capizzano, E. Iuliano, A eulerian method for water droplet impingement by means of an immersed boundary technique, Journal of Fluids Engineering, Transactions of the ASME 136 (4) (2014).

[17] I. Kim, N. Bachchan, O. Peroomian, Supercooled large droplet modeling for aircraft icing using an eulerian-eulerian approach, Journal of Aircraft 53 (2) (2016) 487–500. doi:10.2514/1.C033506.

[18] F. Morency, H. Beaugendre, W. Habashi, Fensap-ice : Effect of ice shapes on 3d eulerian droplet impingement, Tech. Rep. AIAA-2003-1223, American Institute of Aeronautics and Astronautics (2003). doi:http://dx.doi.org/10.2514/6.2003-1223.

[19] R. J. Leveque, The dynamics of pressureless dust clouds and delta waves, Journal of Hyperbolic Differential Equations 1 (2) (2004) 315–327. doi:https://doi.org/10.1142/S0219891604000135.

[20] S.-J. Paardekooper, G. Mellema, Dust flow in gas disks in the presence of embedded planets, Astronomy & Astrophysics 453 (2006) 1129–1140. doi:http://dx.doi.org/10.1051/0004-6361:20054449.

[21] F. Bouchut, S. Jin, X. Li, Numerical approximations of pressureless and isothermal gas dynamics, SIAM Journal of Numerical Analysis 41 (1) (2003) 135–158.

[22] C. Berthon, M. Breuß, M.-O. Titeux, A relaxation scheme for the approximation of the pressureless euler equations, Numerical Methods for Partial Differential Equations 22 (2) (2006). doi:https://doi.org/10.1002/num.20108.

[23] G.-S. Jiang, E. Tadmor, Nonoscillatory central schemes for multidimensional hyperbolic conservation laws, SIAM Journal on Scientific Computing 19 (6) (1998) 1892–1917. arXiv:https://doi.org/10.1137/S106482759631041X, doi:10.1137/S106482759631041X.
URL https://doi.org/10.1137/S106482759631041X

[24] N. K. Garg, M. Junk, S. V. R. Rao, M. Sekhar, An upwind method for genuine weakly hyperbolic systems, arXiv: Numerical Analysis (2017).

[25] N. K. Garg, A class of upwind methods based on generalized eigenvectors for weakly hyperbolic systems, Numerical Algorithms 83 (3) (2020) 1091–1121. doi:10.1007/s11075-019-00717-7.
URL https://doi.org/10.1007/s11075-019-00717-7

[26] T. A. Smith, D. J. Petty, C. Pantano, A roe-like numerical method for weakly hyperbolic systems of equations in conservation and non-conservation form, Journal of Computational Physics 316 (2016) 117–138. doi:http://dx.doi.org/10.1016/j.jcp.2016.04.006.

[27] S. Keita, Y. Bourgault, Eulerian models with particle pressure for air-particle flows, European Journal of Mechanics B-Fluids 78 (2019) 263–275. doi:10.1016/j.euromechflu.2019.08.001.
URL <Go to ISI>://WOS:000491300800024

[28] S. K. Jung, R. S. Myong, A second-order positivity-preserving finite volume upwind scheme for air-mixed droplet flow in atmospheric icing, Computers & Fluids 86 (2013) 459–469. doi:http://dx.doi.org/10.1016/j.compfluid.2013.08.001.

[29] P. Janhunen, A positive conservative method for magnetohydrodynamics based on hll and roe methods, Journal of Computational Physics 160 (2) (2000) 649–661. doi:https://doi.org/10.1006/jcph.2000.6479.
URL https://www.sciencedirect.com/science/article/pii/S0021999100964799

[30] O. Ejtehadi, E. Mahravan, I. Sohn, Investigation of shock and a dust cloud interaction in eulerian framework using a newly developed openfoam solver, International Journal of Multiphase Flow 145 (2021) 103812. doi:https://doi.org/10.1016/j.ijmultiphaseflow.2021.103812.
URL https://www.sciencedirect.com/science/article/pii/S0301932221002445

[31] G. Gallice, A. Chan, R. Loubère, P.-H. Maire, Entropy stable and positivity preserving Godunov-type schemes for multidimensional hyperbolic systems on unstructured grid, Journal of Computational Physics 468 (2022). doi:https://doi.org/10.1016/j.jcp.2022.111493.

[32] R. L. V. Delmas, P.-H. Maire, Revisiting riemann solvers in the lagrangian and eulerian frameworks and their associated numerical methods in 3d, preprint (2024).

[33] J. Quirk, A contribution to the great Riemann solver debate, Int. J. Numer. Methods Fluids 18 (1994) 555–574.

[34] J. J. Quirk, A contribution to the great riemann solver debate, in: M. Y. Hussaini, B. van Leer, J. Van Rosendale (Eds.), Upwind and High-Resolution Schemes, Springer Berlin Heidelberg, pp. 550–569.

[35] S. Keita, Y. Bourgault, Eulerian droplet model: Delta-shock waves and solution of the riemann problem, Journal of Mathematical Analysis and Applications 472 (2019) 1001–1027. doi:https://doi.org/10.1016/j.jmaa.2018.11.061.

[36] G. Gallice, Positive and Entropy Stable Godunovov-Type Schemes for Gas Dynamics and MHD Equations in Lagrangian or Eulerian Coordinates, Numer. Math. 94 (4) (2003) 673–713.

[37] A. Chan, G. Gallice, R. Loubère, P.-H. Maire, Positivity preserving and entropy consistent approximate riemann solvers dedicated to the high-order MOOD-based finite volume discretization of lagrangian and eulerian gas dynamics, Computers & Fluids 229 (2021) 105056.

[38] E. F. Toro, Riemann solvers and numerical methods for fluid dynamics : a practical introduction, 2nd Edition, Springer-Verlag, Berlin, Allemagne, 1999.

[39] M. Pandolfi, D. D'Ambrosio, Numerical Instabilities in Upwind Methods: Analysis and Cures for the Carbuncle Phenomenon, Journal of Computational Physics 166 (2) (2001) 271–301.

[40] A. Rodionov, Artificial viscosity Godunov-type schemes to cure the carbuncle phenomenon, Journal of Computational Physics 345 (2017) 308–329.

[41] P. Maire, A high-order cell-centered Lagrangian scheme for two-dimensional compressible fluid flows on unstructured meshes., Journal of Computational Physics 228 (2009) 2391–2425.

[42] Z. Shen, W. Yan, G. Yuan, A robust and contact resolving Riemann solver on unstructured mesh, Part I, Euler method, Journal of Computational Physics 268 (2014) 432–455.

[43] A. Del Grosso, A. Chan, M. J. Castro, G. Gallice, R. Loubère, P.-H. Maire, A well-balanced and positive finite volume scheme for Shallow-Water equations in multi-dimensions for unstructured grids derived from Lagrangian roots, accepted in Journal of Computational Physics (2023).

[44] P. Jacq, P.-H. Maire and R. Abgrall, A nominally second-order cell-centered finite volume scheme for simulating three-dimensional anisotropic diffusion equations on unstructured grids, Communications in Computational Physics 16 (4) (2014) 841–891. doi:10.4208/cicp.310513.170314a.

[45] P. Jacq, Méthodes numériques de type Volumes Finis sur maillages non structurés pour la résolution de thermique anisotrope et des équations de Navier-Strokes compressibles, PhD thesis University of Bordeaux, 2014.
URL https://www.theses.fr/2014BORD0009